Journal of Hepatocellular Carcinoma

Dovepress
Taylor & Francis Group

Open Access Full Text Article

ORIGINAL RESEARCH

Triphasic CT Radiomics Model for Preoperative Prediction of Hepatocellular Carcinoma Pathological Grading

Haibo Huang[1,*], Xianpan Pan[2,*], Yingdan Zhang[1,*], Jie Yang[1], Lei Chen[2], Qinping Zhao[1], Lifeng Huang[1], Wei Lu[3], Yaohong Deng[2], Yingying Huang[4,*], Ke Ding[1,*]

[1]Department of Radiology, The Third Affiliated Hospital of Guangxi Medical University, Nanning, Guangxi Zhuang Autonomous Region, 530031 People's Republic of China; [2]Shanghai United Imaging Intelligence Co., Ltd., Shanghai, 200232, People's Republic of China; [3]Department of Pathology, The Third Affiliated Hospital of Guangxi Medical University, Nanning, Guangxi, 530031, People's Republic of China; [4]Department of Radiology, The First People's Hospital of Qinzhou, Qinzhou, Guangxi, 530550, People's Republic of China

*These authors contributed equally to this work

Correspondence: Ke Ding, Department of Radiology, The Third Affiliated Hospital of Guangxi Medical University, Nanning, Guangxi Zhuang Autonomous Region, 530031, People's Republic of China, Email 272480365@qq.com; Yingying Huang, Department of Radiology, The First People's Hospital of Qinzhou, Qinzhou, Guangxi, 530031, People's Republic of China, Email 273749105@qq.com

Objective: This study aimed to develop and validate a triphasic CT-based radiomics model for the synchronous prediction of multiple critical pathological markers in hepatocellular carcinoma (HCC).

Materials and Methods: This retrospective study analyzed 174 patients with 187 hepatocellular carcinoma (HCC) lesions. Radiomic features (n = 2264) were extracted from arterial phase (AP), venous phase (VP), and delayed phase (DP) CT images. Key features were selected using minimum redundancy maximum relevance (mRMR), SelectKBest, and least absolute shrinkage and selection operator (LASSO) algorithms. Logistic regression and support vector machine (SVM) classifiers were employed to develop individual phase-specific models and a triphasic fusion model. Model performance was evaluated through the area under the curve (AUC), sensitivity, specificity, decision curve analysis, and other metrics.

Results: The triphasic fusion model demonstrated superior performance. In the testing 1 dataset, the triphasic fusion model achieved AUCs of 0.890 (95% CI: 0.741–1), 0.895 (95% CI: 0.781–1) and 0.829 (95% CI: 0.675–0.984) for Edmondson-Steiner (Ed) grading, Microvascular invasion (MVI) grading, and Satellite nodule (SN) grading, respectively. In the testing 2 (validation) dataset, the triphasic fusion model achieved AUCs of 0.836 (95% CI: 0.739–0.934), 0.871 (95% CI: 0.748–0.993) and 0.810 (95% CI: 0.656–0.963) for Ed, MVI, and SN grading, respectively. The performance of the fusion model was better than that of the single-phase models.

Conclusion: The triphasic CT radiomics model provides a noninvasive tool for preoperative prediction of HCC pathological grading (Ed, MVI, SN), enhancing diagnostic accuracy for clinical decision-making and prognostic evaluation.

Plain Language Summary:

Why is this study important?

- Preoperative prediction of HCC pathological features (Ed, MVI, and SN grading) is clinically significant.
- A triphasic CT-based fusion model demonstrated strong predictive performance:
  - Testing 1 dataset: AUCs of 0.890 (Ed), 0.895 (MVI), and 0.829 (SN) grading.
  - Testing 2 (validation) dataset: AUCs of 0.836 (Ed), 0.871 (MVI), and 0.810 (SN) grading.
- The model aids in preoperative clinical decision-making and prognostic evaluation for HCC patients.

Keywords: pathological grading, hepatocellular carcinoma, contrast-enhanced CT, radiomics

Received: 26 March 2025
Accepted: 11 July 2025
Published: 6 August 2025

Introduction

In 2022, liver cancer ranked as the sixth most commonly diagnosed malignancy globally, with approximately 865,269 new cases reported.[1] China bore the highest disease burden, accounting for nearly half of global cases (411,300 in 2020).[2] Despite advances in surgery, 5-year recurrence rates exceed 70%, due to tumor biological heterogeneity reflected by histopathological markers such as Ed grading, MVI, and SN status.[3–7]

Current preoperative assessments using conventional imaging (eg, contrast-enhanced CT/MRI) focus on evaluating morphological characteristics (eg, tumor size, capsule integrity) but fail to quantitatively predict critical prognostic markers like MVI status or Ed differentiation grading.[8,9] MRI sequences (eg, DWI, DCE-MRI) also have limitations: DWI shows AUCs of 0.70–0.75 for MVI/Ed,[10] while DCE-MRI parameters are protocol-dependent with poor multi-center consistency.[11]

Radiomics, a quantitative imaging tool, extracts subvisual texture features to reflect tumor microenvironment heterogeneity.[12,13] However, prior single-phase radiomic models (eg, MRI arterial phase),[14] single-phase CT[15] show limited performance (AUCs 0.800) due to capturing only one hemodynamic phase. For example, Mao et al reported an AUC of 0.777 for Ed grading);[14] Xia et al achieved 0.760 for MVI;[15] and Wu et al showed 0.750 for Ed with non-contrast MRI.[16]

Triphasic CT captures the dynamic enhancement patterns across arterial (angiogenesis), venous (washout), and delayed (capsular) phases, offering complementary hemodynamic information. Despite this potential, no prior study has integrated triphasic CT radiomics to synchronously predict multiple pathological markers. Clinically, decisions require evaluating Ed (malignancy), MVI (recurrence), and SN (metastasis) together.[4,5,8]

The aim of this study aimed to develop a triphasic CT radiomics model for the first time to synchronously predict Ed grading, MVI, and SN status, providing a comprehensive preoperative assessment tool to improve HCC diagnosis and treatment.

Materials and Methods

Study Population

This retrospective study utilized imaging datasets from two centers, the Third Affiliated Hospital of Guangxi Medical University (Center A) and the First People's Hospital of Qinzhou (Center B), encompassing 187 HCC lesions from 174 patients. For patients with multiple HCC lesions, each lesion was treated as an independent sample. The study was conducted in compliance with the Declaration of Helsinki and approved by the Medical Ethics Committee of the Third Affiliated Hospital of Guangxi Medical University (Approval No.: Y2020036, Date of approval: February 24, 2020), Informed consent was waived by the Ethics Committee due to the retrospective design and the absence of identifiable patient information, ensuring no risk of patient privacy breach. All data were de-identified and securely stored to protect confidentiality. During the data collection process, we retrieved 428 patients from the medical information database of Center A, all of whom were diagnosed with HCC between January 2018 and April 2024. Among these, 210 patients were excluded from the study due to not undergoing iodine agent-enhanced CT imaging prior to surgical resection, 70 patients were excluded for receiving local-regional therapies such as chemoembolization or chemoradiation before surgery, 20 cases of Diffuse HCC lesion were excluded, and 16 patients were excluded due to incomplete pathological records. Ultimately, 112 patients (97 males and 15 females, mean age: 57.3 ± 12.6 years; range: 27–79 years) with a total of 125 HCC nodules were included from this center. Meanwhile, based on the same inclusion and exclusion criteria (Figure 1), we included 62 patients with solitary HCC (48 males and 14 females, mean age: 54.5 ± 12.1 years; range: 30–76 years) from Center B in this study.

The inclusion criteria were as follows: (1) Patients who underwent multiphase contrast-enhanced abdominal CT; (2) Individuals who underwent radical surgical resection resulting in pathological diagnosis of HCC; (3) Patients with complete records of histological pathology including Ed, MVI, SN, respectively.

The exclusion criteria were: (1) Patients who received tumor-related treatment prior to surgery; (2) The original thin data of complete triphase enhanced CT images was not available; (3) Diffuse lesions where boundaries cannot be defined for HCC.

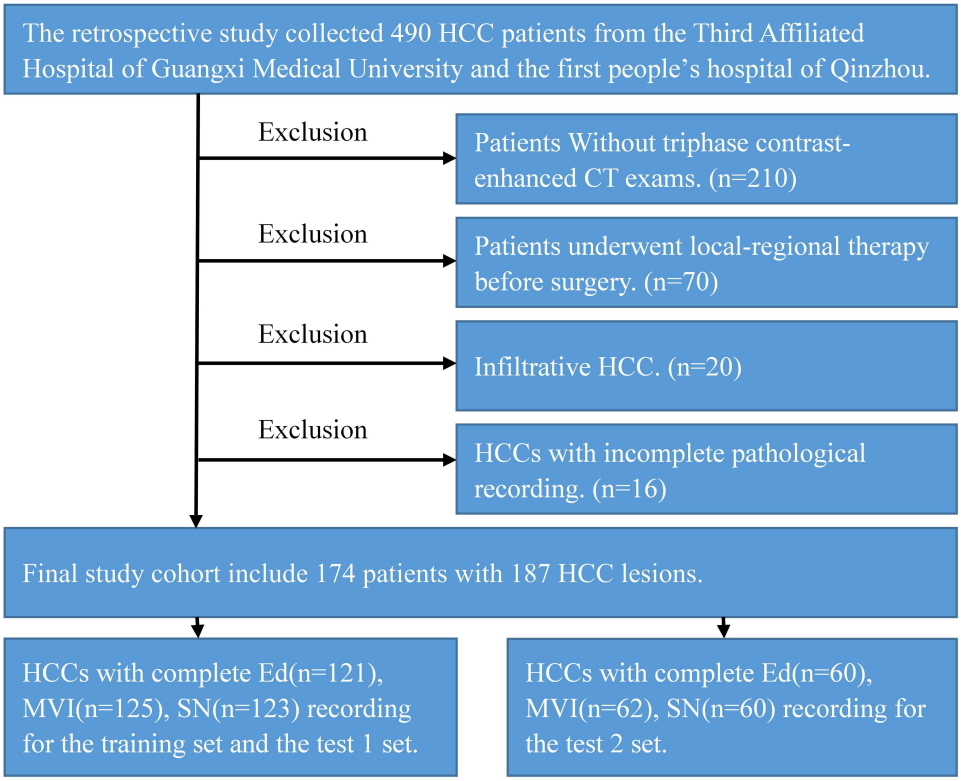

Figure 1 Flowchart of the study includes HCC patients enrolled with triphasic contrast-enhanced CT images and pathological grading records.

Datasets

In this retrospective study, HCC lesions with complete histopathological grading records were categorized into three datasets based on Ed grading, MVI and SN status, namely the training set, the testing 1 set, and the testing 2 (validation) set. Specifically, for the Ed grading task include 96 training cases, 25 testing 1 cases and 60 testing 2 (validation) cases. The MVI status task comprised 120 training cases, 31 testing 1 cases, and 36 testing 2 (validation) cases. The SN status task consisted of 120 training cases, 31 testing 1 cases, and 32 testing 2 (validation) cases. The demographic characteristics (age, gender), clinical indicators (tumor volume), and pathological features (Ed grading, MVI status, SN status) of the groups are shown in Table 1 (stratified by Ed grading), Table 2 (validation) (stratified by MVI status), and Table 3 (stratified by SN status), respectively.

Table 1 Baseline Demographic Characteristics of Patients Stratified by Ed Status

Characteristics	Ed Grade I–II (n = 95)	Ed Grade III–IV (n = 86)	*P*-value
Age (Mean ± SD)	56.295 ± 12.375	57.151 ± 11.429	0.630
Gender (%)			0.508
Male	82 (86.316)	77 (89.535)	
Female	13 (13.684)	9 (10.465)	
MVI status (%)			<0.01
M0	44 (46.316)	8 (9.302)	
M1	43 (45.263)	28 (32.558)	
M2	8 (8.421)	50 (58.140)	
SN status (%)			<0.01
Negative	72 (75.789)	20 (23.256)	
Positive	23 (24.211)	66 (76.744)	
Tumor volume (cm^3) (Median[Q1, Q3])	26.337 [6.533, 114.862]	115.718 [37.537, 299.152]	<0.01

Notes: "n.": number; Q1, Q3 mean the first and third quartile respectively.
Abbreviations: MVI, Microvascular invasion; Ed, Edmondson-Steiner; SN, Satellite nodule.

https://doi.org/10.2147/JHC.S527056

Table 2 Baseline Demographic Characteristics of Patients Stratified by MVI Status

Characteristics	Absence of MVI in HCC (n = 51)	HCC with MVI (n = 136)	*P*-value
Age (Mean ± SD)	56.784 ± 9.991	56.316 ± 12.391	0.864
Gender (%)			0.026
Male	41 (80.392)	125 (91.912)	
Female	10 (19.608)	11 (8.088)	
Ed grading (%)			<0.01
Grade I	23 (45.098)	7 (5.147)	
Grade II	21 (41.176)	48 (35.294)	
Grade III	6 (11.765)	60 (44.118)	
Grade IV	1 (1.961)	21 (15.441)	
SN status (%)			<0.01
Negative	47 (92.157)	47 (34.559)	
Positive	4 (7.843)	89 (65.441)	
Tumor volume (cm^3) (Median[Q1, Q3])	10.177 [5.204,28.267]	106.108 [31.353, 297.654]	<0.01

Notes: "n.": number; Q1, Q3 mean the first and third quartile respectively.
Abbreviations: MVI, Microvascular invasion; Ed, Edmondson-Steiner; SN, Satellite nodule.

Table 3 Baseline Demographic Characteristics of Patients Stratified by Satellite Nodules Status

Characteristics	Absence of SN (n = 96)	Presence of SN (n = 87)	*P*-value
Age (Mean ± SD)	55.250 ± 11.928	57.943 ± 11.815	0.127
Gender (%)			0.042
Male	80 (83.333)	81 (93.103)	
Female	16 (16.667)	6 (6.897)	
Ed status (%)			<0.01
Grade I	25 (26.042)	6 (6.897)	
Grade II	51 (53.125)	18 (20.690)	
Grade III	14 (14.583)	48 (55.172)	
Grade IV	6 (6.250)	15 (17.241)	
MVI status (%)			<0.01
M0	50 (52.083)	4 (4.598)	
M1	43 (44.792)	30 (34.483)	
M2	3 (3.125)	53 (60.920)	
Tumor volume (cm^3) (Median[Q1, Q3])	27.604 [6.834, 123.322]	111.447 [36.830, 298.403]	<0.01

Note: "n.": number; Q1, Q3 mean the first and third quartile respectively.
Abbreviations: MVI, Microvascular invasion; Ed, Edmondson-Steiner; SN, Satellite nodule.

Histopathological Classification

The histopathological evaluation of HCC was performed according to established diagnostic criteria:[17,18]

Differentiation Grade Was Categorized Using the Ed Classification System

- Class 0: Well-to-moderately differentiated (Ed I–II)
- Class 1: Poorly differentiated (Ed III–IV)

MVI Status Was Determined Through Histopathological Confirmation

- Negative (Grade 0): No evidence of vascular invasion
- Positive: Any degree of invasion (Grades 1–2, including low-risk and high-risk subgroups)

SN Status Were Classified as

- Negative: No peritumoral satellite lesions within 2 cm of the main tumor
- Positive: Presence of ≥1 histologically confirmed satellite nodule

Table 4 Contrast-Enhanced CT Protocol of Two Center

• **Center A** (The Third Affiliated Hospital of Guangxi Medical University)	• **Center B** (the First People's Hospital of Qinzhou)
• **Scanner**: 64-slice multidetector CT (Discovery^{TM} CT 750HD, GE Healthcare)	• **Scanner**: 64-row dual-source CT (SOMATOM Definition Flash, Siemens Healthineers)
• **Contrast protocol**: ○ Non-ionic iodinated contrast agent (320–370 mg I/mL) ○ Individualized dose based on body weight (400 mg I/kg) ○ Injection rate: 2.6–5.9 mL/s via cubital vein using a dual-chamber injector (Optivantage, Liebel-Flarsheim Company, LCC, Cincinnati OH, USA) ○ Post-contrast saline flush: 30–50 mL at equivalent flow rate	• **Contrast protocol**: ○ Iodofol 350 mg I/mL (Jiangsu Hengrui Medicine Co., Ltd.) ○ Fixed dose scheme: 1.5 mL/kg body weight ○ Injection rate: 3.0 mL/s via cubital vein using a dual-chamber injector (Accutron CT-D862, Shanghai Gaolang Co., LTD., China). ○ Post-contrast saline flush: 30–50 mL at equivalent flow rate
• **Scan phases**: ○ Arterial phase (AP): 30–35s (with bolus-triggered monitoring of abdominal aorta at 150–180 HU, AP was obtained when reaching a threshold of 150–180Hu, and delayed 10–13s) ○ Portal venous phase (VP): 60s ○ Delayed phase (DP): 180s	• **Scan phases**: ○ Arterial phase (AP): 20–25s (fixed-delay based on test bolus) ○ Portal venous phase (VP): 60s ○ Delayed phase (DP): 120s
• **Reconstruction**: Axial slices at 1.25 mm thickness, DICOM format	• **Reconstruction**: Thin-slice images at 1.0 mm thickness, DICOM format

Contrast-Enhanced CT Protocol

The contrast-enhanced CT acquisition parameters for the two centers are summarized and compared in Table 4.

To ensure consistency between the two centers, all CT images were first normalized to a standard abdominal window (window width: 300 HU, window level: 40 HU). Subsequently, images were resampled to an isotropic voxel size of 1.0 × 1.0 × 1.0 mm³ using linear interpolation, in order to reduce variability in voxel spacing and enable reproducible radiomic feature extraction. This standardization process may help to reduce the impact of heterogeneity in multi-center CT data.

Tumor Segmentation and Radiomic Analysis

The analytical workflow of this study is illustrated in Figure 2, encompassing tumor ROI segmentation, radiomics feature extraction, feature selection, classification model construction, and model evaluation.

Tumor Segmentation

Three-phase (AP/VP/DP) CT images were independently annotated by two board-certified abdominal radiologists (with 8 and 10 years of experience) using dedicated software (3DSlicer, v5.2.2). Tumor region of interest (ROI) was manually segmented along the tumor margins, excluding adjacent vessels and necrotic areas (Figure 3).

Interobserver Consistency Assessment

- A randomly selected subset (n = 30) underwent duplicate segmentation by both radiologists under blinded conditions
- Spatial consistency was quantified using the Dice similarity coefficient (DSC)
- Feature stability was evaluated through intraclass correlation coefficient (ICC) analysis

Quality Control Criteria

- Acceptable spatial agreement: DSC ≥ 0.85.
- Feature retention threshold: ICC ≥ 0.75 (2084 out of 2264).
- Discrepant segmentations (DSC < 0.85) were resolved by consensus review.

Feature Extraction and Selection

Features Extraction

A total of 2264 radiomic features were extracted by uAI Research Portal (version 20240730) from each HCC region.

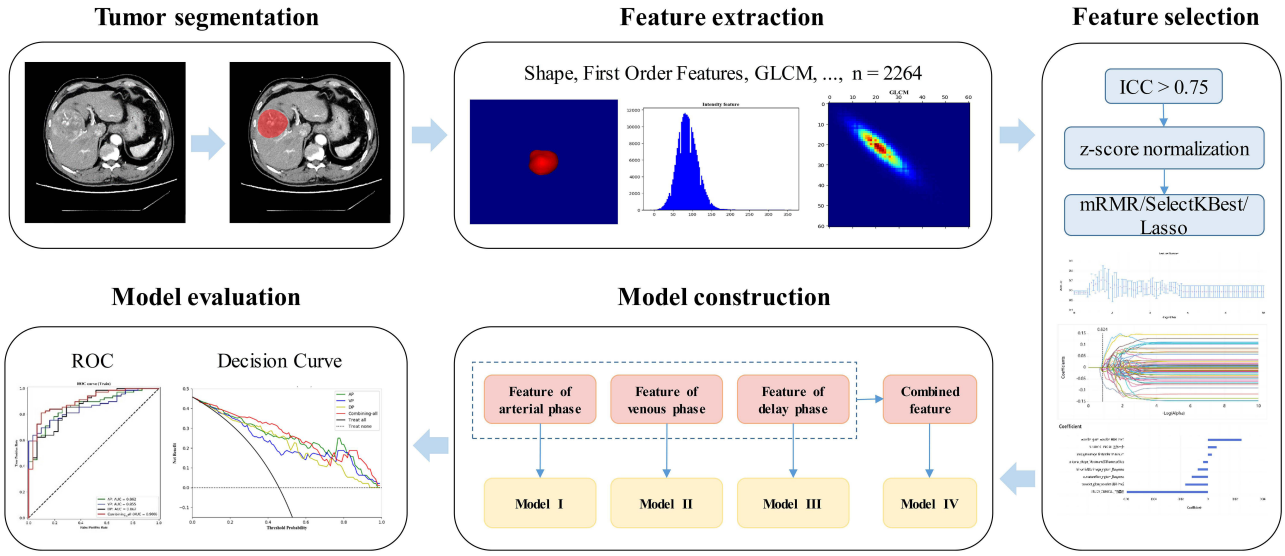

Figure 2 Flowchart of tumor segmentation and radiomic analysis on multi-phase CT images.

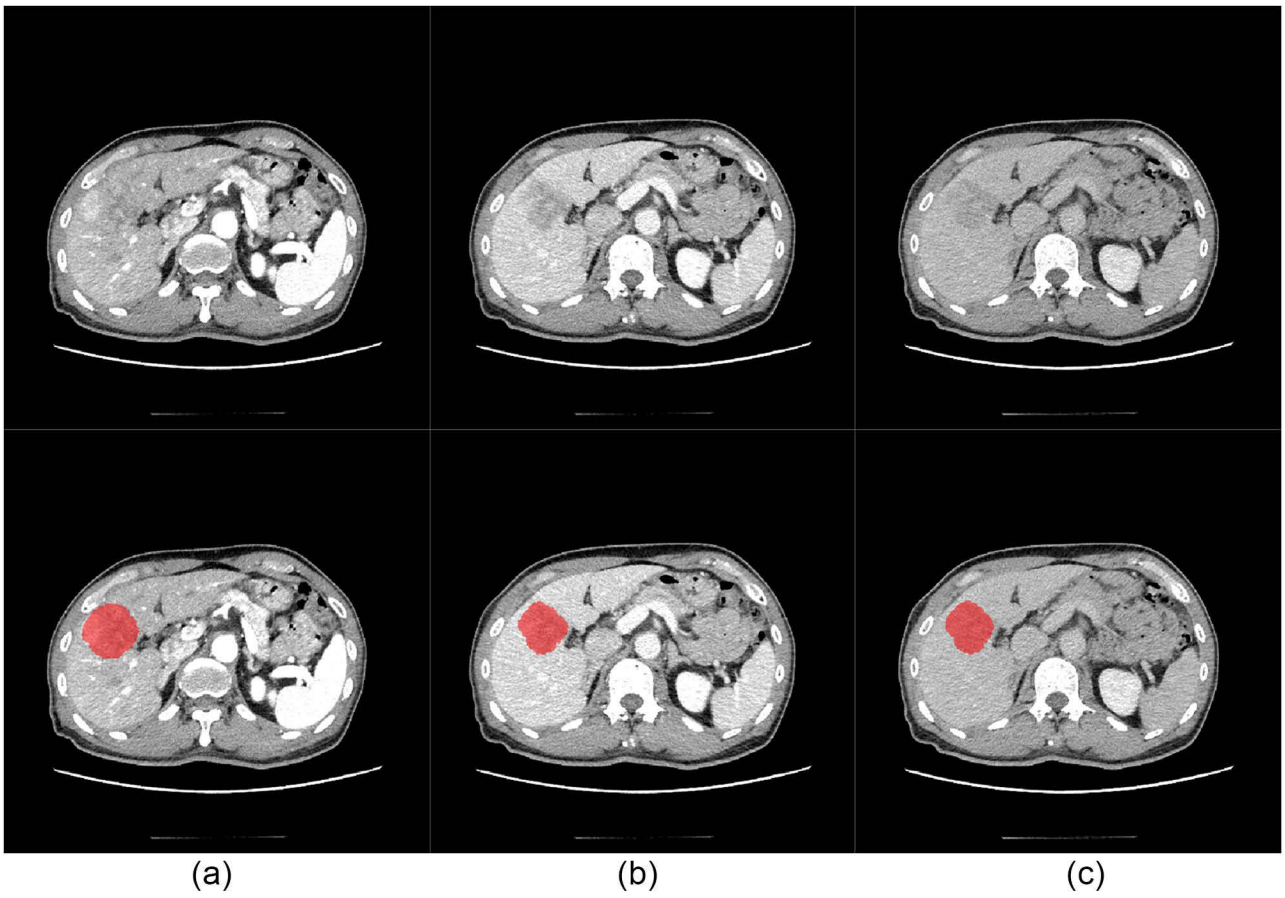

Figure 3 Illustration of contrast-enhanced CT images the delineations (top: original image, bottom: delineations) of a HCC patient. (**a**) arterial phase, (**b**) venous phase, (**c**) delayed phase.

These features comprised 104 original features, which were further classified into 18 first-order statistics, 14 shape features, and 21 texture features. The texture features encompassed Gray-Level Co-occurrence Matrix (GLCM), Gray-Level Run-Length Matrix (GLRLM), Gray-Level Size-Zone Matrix (GLSZM), Gray-Level Dependence Matrix

(GLDM), and Neighboring Gray-Tone Difference Matrix (NGTDM). Additionally, a set of 14 image filters including Box Mean, Additive Gaussian Noise, Binomial Blur Image, Curvature Flow, Box Sigma Image and Laplacian of Gaussian were applied to generate derived images. Derived images underwent further processing using Wavelet filters (LLL, LLH, LHL, LHH, HLL, HLH, HHL, HHH), Normalize, Laplacian Sharpening, Discrete Gaussian Mean Speckle Noise Recursive Gaussian and Shot Noise to extract first-order statistics and texture features within the HCC regions. This resulted in a total of 2264 derived features.

Features Selection

After extracting radiomics features from the tumor ROI on CT images, a series of feature dimensionality reduction methods were employed to select stable and highly relevant features for the classification task. Firstly, features with an ICC ≥ 0.75 in test–retest evaluations were identified as reproducible Radiomic features. Then the mRMR, SelectKBest, and LASSO selection algorithms were employed to identify the most robust predictive radiomic features.

Model Construction and Evaluation

The radiomic features were selected using the mRMR, SelectKBest and LASSO techniques, followed by building classifiers. For model construction, LASSO Logistic regression was used for Ed grading prediction, while SVM was applied for MVI and SN status prediction. This choice was based on LASSO's strength in linear feature modeling (aligned with Ed grading's linear association with radiomic features) and SVM's capability to capture non-linear relationships (critical for MVI/SN prediction). Four models were constructed: three models utilizing radiomic features extracted from arterial, venous, and delay phases, respectively, and a combined model incorporating all selected features extracted from triphasic images. These models were employed to synchronously predict three pathological characteristics: Ed, MVI, and SN grading. The performance of the prediction models was evaluated using receiver operating characteristic (ROC) curves. To optimize performance, a grid search was conducted to fine-tune parameters for different features and classification algorithms.

The prediction model's performance was evaluated with ROC curves, calculating sensitivity (SEN), specificity (SPE), accuracy (ACC), F1-Score, and AUC. Demographic data were analyzed via the uAI Research Portal to compare variables between training, testing 1 and testing 2 (validation) sets. Model testing 1 and testing 2 (validation) and statistical analysis were performed in Python 3.6. Actual vs predicted grading was assessed with the Hosmer–Lemeshow test, and calibration curves were created. Decision curves quantified the Radiomics models' clinical utility across various risk thresholds.

Results

Stratified Analysis Revealed Significant Associations Across Pathological Grading Groups (Tables 1–3)

- Compared with the Ed I–II group, the Ed III–IV group showed a higher proportion of MVI M2 grade (58.1% vs 8.4%, $P < 0.01$), higher SN positivity rate (76.7% vs 24.2%, $P < 0.01$), and larger tumor volume (115.7 cm^3 vs 26.3 cm^3, $P < 0.01$).
- The MVI-positive group had a higher male proportion (91.9% vs 80.4%, $P = 0.026$), higher Ed III–IV grade proportion (59.6% vs 13.7%, $P < 0.01$), higher SN positivity rate (65.5% vs 7.8%, $P < 0.01$), and larger tumor volume (106.1 cm^3 vs 10.2 cm^3, $P < 0.01$) than the MVI-negative group.
- The SN-positive group exhibited a higher male proportion (93.1% vs 83.3%, $P = 0.042$), higher Ed III–IV grade proportion (72.4% vs 20.8%, $P < 0.01$), higher MVI M2 grade proportion (60.9% vs 3.1%, $P < 0.01$), and larger tumor volume (111.4 cm^3 vs 27.6 cm^3, $P < 0.01$) compared with the SN-negative group.

Feature Extraction and Selection Results

According to Harrell's guideline, the number of selected features should be less than 10% of the sample size. Consequently, in our experiment involving the radiomic features, as well as their combined analysis, the number of selected features adhered to this criterion by being less than 10% of the sample size.

We initially extracted 2264 radiomic features from tumor regions. After intra-cohort correlation analysis with a 0.75 threshold, reproducible features were reduced to 2084. Feature selection methods (mRMR, SelectKBest, and LASSO) identified 6–10 features from AP, VP and DP. Additionally, we selected 6–12 features from the three phases (AP, VP, and DP) for subsequent combined model construction. The relevance of the selected features to the classification task and their importance coefficients are detailed in Figures 4–6 and Supplementary Material.

Performance of Radiomics Models

The feature selection process automatically identified the most significant features for the classification task. Subsequently, the Logistic regression and support vector machine classifiers were used to build the detection model. The overall performance of the prediction models was evaluated by computing mean AUC, sensitivity, specificity, accuracy, and F1 score for the training, testing 1 and testing 2 (validation) sets. The Ed classification model (using LASSO Logistic regression) demonstrates better predictive efficiency compared to other models, with combined model AUSs of 0.890 (testing 1) and 0.836 (testing 2). For MVI and SN status, SVM-based models achieved combined model AUCs of 0.895 (testing 1) and 0.871 (testing 2) for MVI, and 0.829 (testing 1) and 0.810 (testing 2) for SN, respectively. The performance of the combined model generally surpasses that of single-phase models. Tables 5–7 summarize the detailed performance metrics (including sensitivity, specificity, and accuracy) of the Ed, MVI, and SN classification models, respectively.

As depicted in Figure 7, the ROC curves of the Ed, MVI, and SN models indicate that the combined models exhibited superior performance. The calibration curves demonstrated a closer alignment between the predictive model and the actual grading in both the testing 1 set and the testing 2 cohort (Figure 8). The decision curves show that the combined models provided a higher net benefit compared to the single-sequence Radiomics model (Figure 9). The triphasic fusion model demonstrated potential to guide personalized surgical planning by noninvasively identifying high-risk HCC subtypes. This noninvasive approach could inform decisions on resection margins and adjuvant therapy selection, addressing a critical unmet need in HCC management.

Based on decision curve analysis (DCA, Figure 9), the triphasic fusion model demonstrated 8–12% higher net benefit than single-phase models (AP/VP/DP) for Ed grading prediction when the threshold probability ranged from 5% to 60%. For MVI prediction, the net benefit of the fusion model was 15% higher than single-phase models when the threshold probability exceeded 20% (corresponding to a reduction of approximately 10% in unnecessary surgery). This advantage is highly consistent with Chinese Expert Consensus (2024 edition)[18] organized and developed by Chinese Medical Association Liver Cancer Professional Committee that "MVI-positive patients require extended resection margins (≥1 cm) to reduce recurrence".

Important Radiomics Features of Model Building

Key features (6–12) were selected using mRMR, SelectKBest, and LASSO regression to construct phase-specific (arterial, venous, delayed) and triphasic fusion models for predicting Ed grading, MVI and SN status in HCC. The specific features are as follows (feature weight coefficients are detailed in Figures 4–6).

For Ed Grading Prediction

- AP model: Includes features such as 3D-Kurtosis, ZonePercentage, and GrayLevelNonUniformityNormalized.
- VP model: Incorporated features like recursivegaussian_gldm_SmallDependenceEmphasis, original_glszm_ZoneEntropy, and shotnoise_glcm_Idn.
- DP model: Utilized features including recursivegaussian_glszm_ZonePercentage, wavelet_glszm_wavelet-HLL-LargeAreaLowGrayLevelEmphasis, and SizeZoneNonUniformityNormalized.
- Triphasic fusion model: Integrated key features such as wavelet_glszm_wavelet-LHL-GrayLevelNonUniformityNormalized_AP, original_glszm_ZoneEntropy_VP, and recursivegaussian_glszm_Zone Percentage_DP.

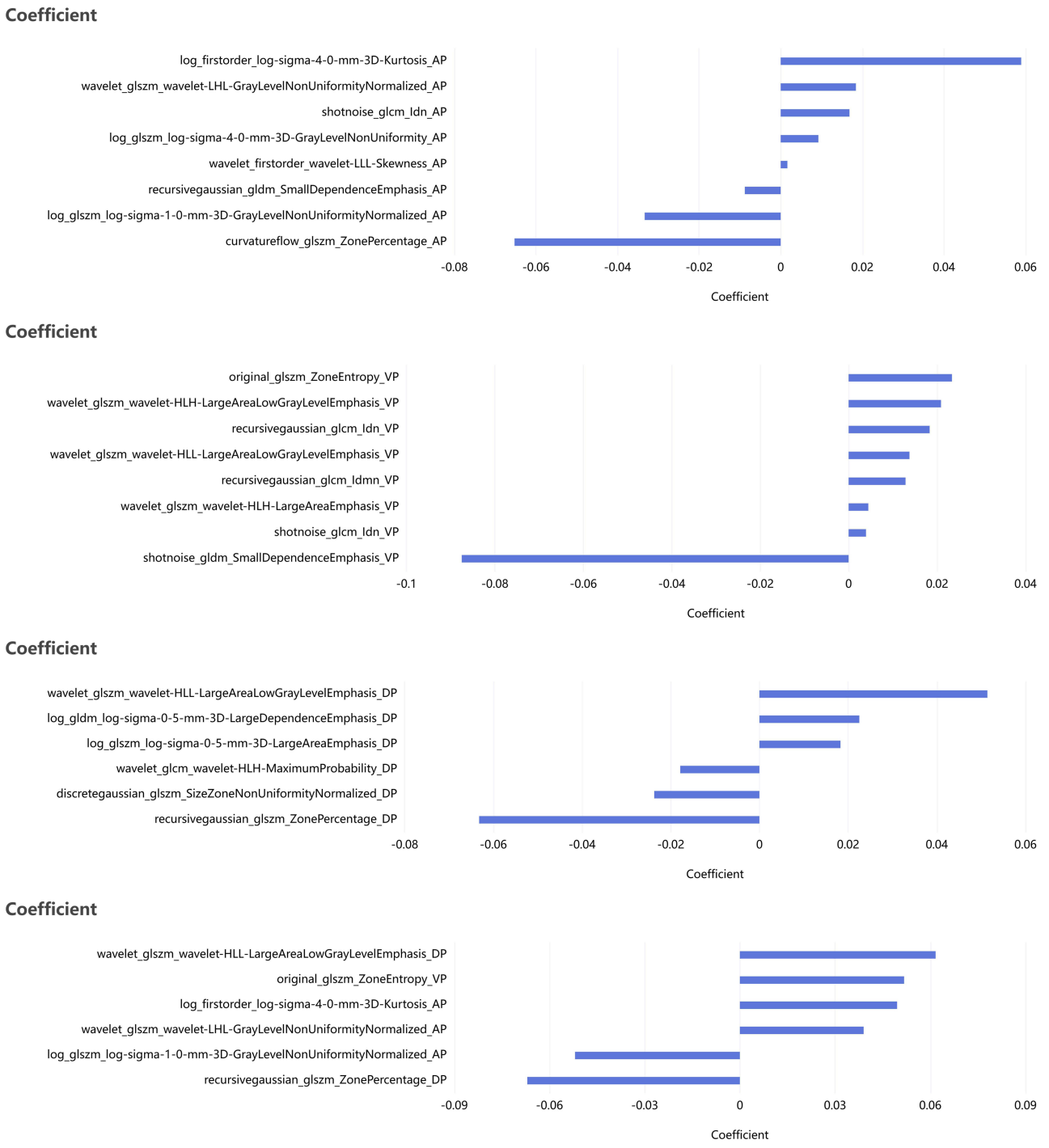

Figure 4 LASSO feature importance analysis constructed for AP, VP, DP and Combined Ed models (from top to bottom).

For MVI Prediction

- AP model: Includes features like wavelet_gldm_wavelet-HHL-DependenceEntropy, laplaciansharpening_firstorder_Range, and additivegaussiannoise_firstorder_Maximum.
- VP model: Utilizes features like original_shape_Maximum2DDiameterSlice, laplaciansharpening_glrlm_Short RunLowGrayLevelEmphasis, and binomialblurimage_glcm_Idn.
- DP model: incorporates features including original_shape_Maximum2DDiameterSlice, laplaciansharpening_ firstorder_Range, and specklenoise_glrlm_RunEntropy.

https://doi.org/10.2147/JHC.S527056

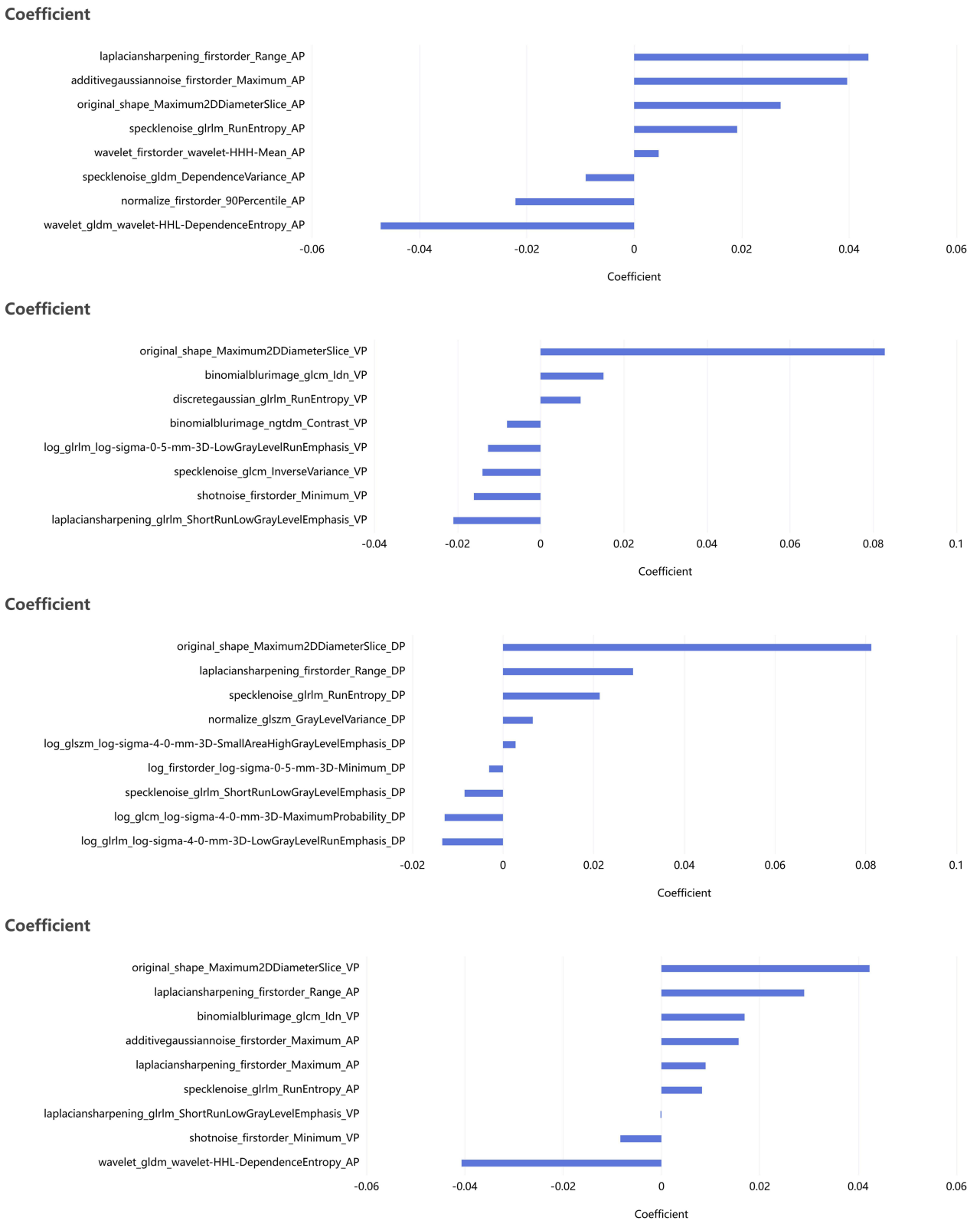

Figure 5 LASSO feature importance analysis constructed for AP, VP, DP and Combined MVI models (from top to bottom).

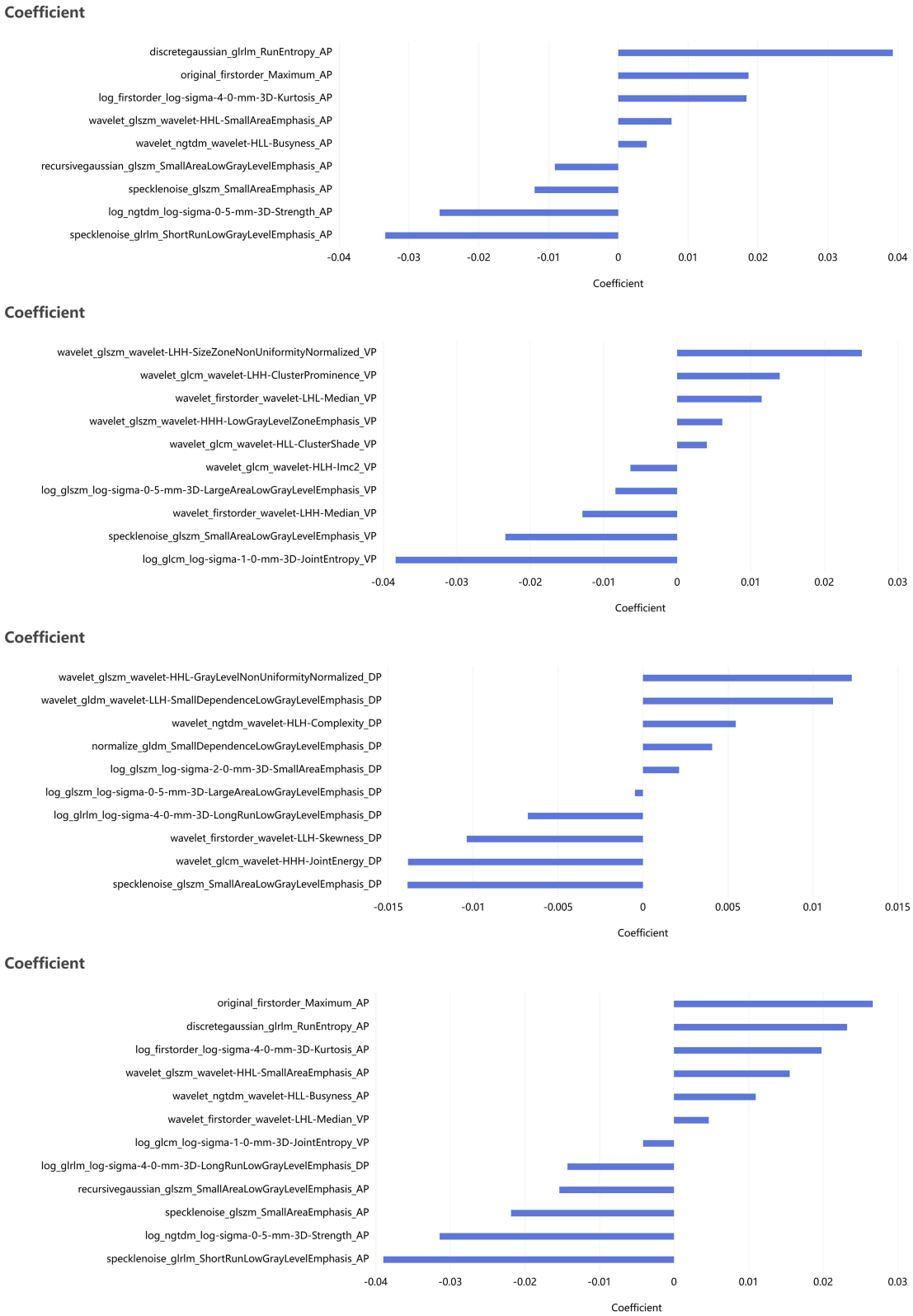

Figure 6 LASSO feature importance analysis constructed for AP, VP, DP and Combined SN models (from top to bottom).

https://doi.org/10.2147/JHC.S527056

Table 5 Performance of LASSO Logistic Regression Classifier-Based Ed Models

Models	AUC (95% CI)			Sensitivity			Specificity			Accuracy			F1 Score		
	Train	Test 1	Test 2	Train	Test 1	Test 2	Train	Test 1	Test 2	Train	Test 1	Test 2	Train	Test 1	Test 2
AP	0.887 (0.823–0.950)	0.838 (0.670–1)	0.784 (0.666–0.902)	0.795	0.727	0.871	0.788	0.786	0.586	0.792	0.760	0.733	0.778	0.727	0.771
VP	0.830 (0.750–0.909)	0.825 (0.639–1)	0.819 (0.713–0.924)	0.659	0.818	1	0.788	0.714	0.138	0.729	0.760	0.583	0.690	0.750	0.713
DP	0.873 (0.806–0.940)	0.766 (0.551–0.982)	0.474 (0.325–0.623)	0.795	0.727	0.097	0.769	0.786	1	0.781	0.760	0.533	0.769	0.727	0.176
Combined	0.901 (0.841–0.961)	0.890 (0.741–1)	0.836 (0.739–0.934)	0.818	0.818	1	0.808	0.786	0.414	0.812	0.800	0.717	0.800	0.783	0.785

Notes: AP, VP, DP are the abbreviation from arterial phase, venous phase and delayed phase, respectively. AUC is the abbreviation from area under the curve. 95% CI means 95% confidence interval.

Table 6 Performance of Support Vector Machine Classifier-Based MVI Models

Models	AUC (95% CI)			Sensitivity			Specificity			Accuracy			F1 Score		
	Train	Test 1	Test 2	Train	Test 1	Test 2	Train	Test 1	Test 2	Train	Test 1	Test 2	Train	Test 1	Test 2
AP	0.924 (0.877–0.970)	0.868 (0.740–0.996)	0.853 (0.722–0.984)	0.899	0.850	0.821	0.683	0.727	0.625	0.825	0.806	0.778	0.871	0.850	0.852
VP	0.918 (0.866–0.969)	0.864 (0.730–0.997)	0.772 (0.606–0.939)	0.886	0.900	0.893	0.707	0.727	0.375	0.825	0.839	0.778	0.870	0.878	0.862
DP	0.872 (0.809–0.935)	0.805 (0.638–0.971)	0.781 (0.587–0.975)	0.835	0.700	0.857	0.707	0.727	0.625	0.792	0.710	0.806	0.841	0.757	0.873
Combined	0.940 (0.900–0.980)	0.895 (0.781–1)	0.871 (0.748–0.993)	0.886	0.850	0.857	0.756	0.818	0.625	0.842	0.839	0.806	0.881	0.872	0.873

Note: The abbr. same as Table 5.

Table 7 Performance of Support Vector Machine Classifier-Based Satellite Nodule Models

Models	AUC (95% CI)			Sensitivity			Specificity			Accuracy			F1 Score		
	Train	Test 1	Test 2	Train	Test 1	Test 2	Train	Test 1	Test 2	Train	Test 1	Test 2	Train	Test 1	Test 2
AP	0.796 (0.718–0.874)	0.775 (0.605–0.945)	0.789 (0.631–0.948)	0.763	0.667	0.923	0.607	0.750	0.632	0.683	0.710	0.750	0.703	0.690	0.750
VP	0.765 (0.681–0.848)	0.617 (0.408–0.825)	0.632 (0.419–0.844)	0.627	0.667	0.462	0.803	0.625	0.789	0.717	0.645	0.656	0.685	0.645	0.522
DP	0.718 (0.626–0.810)	0.712 (0.528–0.897)	0.640 (0.425–0.854)	0.627	0.667	0.462	0.656	0.625	0.842	0.642	0.645	0.688	0.632	0.645	0.545
Combined	0.832 (0.759–0.904)	0.829 (0.675–0.984)	0.810 (0.656–0.963)	0.729	0.667	0.692	0.705	0.812	0.789	0.717	0.742	0.750	0.717	0.714	0.692

Note: The abbr. same as Table 5.

- Triphasic fusion model: integrates key features such as original_shape_Maximum2DDiameterSlice_VP, wavelet_gldm_wavelet-HHL-DependenceEntropy_AP, and laplaciansharpening_firstorder_Range_AP.

For SN Prediction

- AP model: Includes features like specklenoise_glrlm_RunEntropy, specklenoise_glrlm_ShortRunLowGrayLevelEmphasis, and log_ngtdm_log-sigma-0-5-mm-3D-Strength.
- VP model: Utilizes features such as log_glcm_log-sigma-1-0-mm-3D-JointEntropy, wavelet_glszm_LHH-SizeZoneNonUniforityNormalized, and specklenoise_glszm_SmallAreaLowGrayLevelEmphasis.
- DP model: Incorporated features including specklenoise_glszm_SmallAreaLowGrayLevelEmphasis, wavelet_glcm_wavelet-HHH-JointEnergy, and wavelet_glszm_wavelet-HHL-GrayLevelNonUniformityNormalized.
- Triphasic fusion model: Integrated features such as specklenoise_glrlm_ShortRunLowGrayLevelEmphasis_AP, wavelet_firstorder_wavelet-LHL-Median_VP, and log_glrlm_log-sigma-4-0-mm-3D-LongRunLowGrayLevelEmphasis_DP.

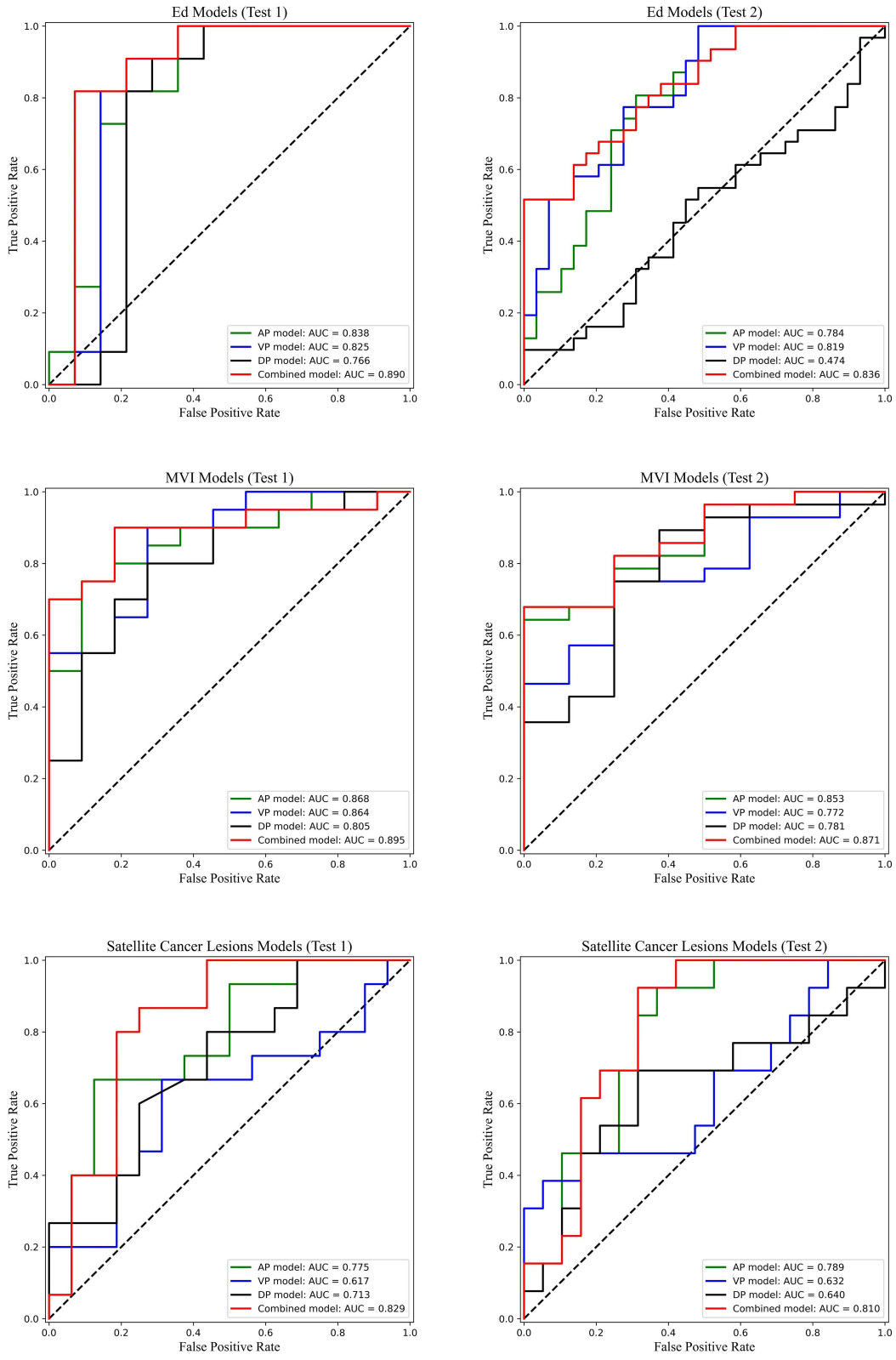

Figure 7 The ROC curves of different models on test 1 and test 2 datasets. The models for Ed grading, MVI grading, and SN grading (from top to bottom), respectively.

https://doi.org/10.2147/JHC.S527056

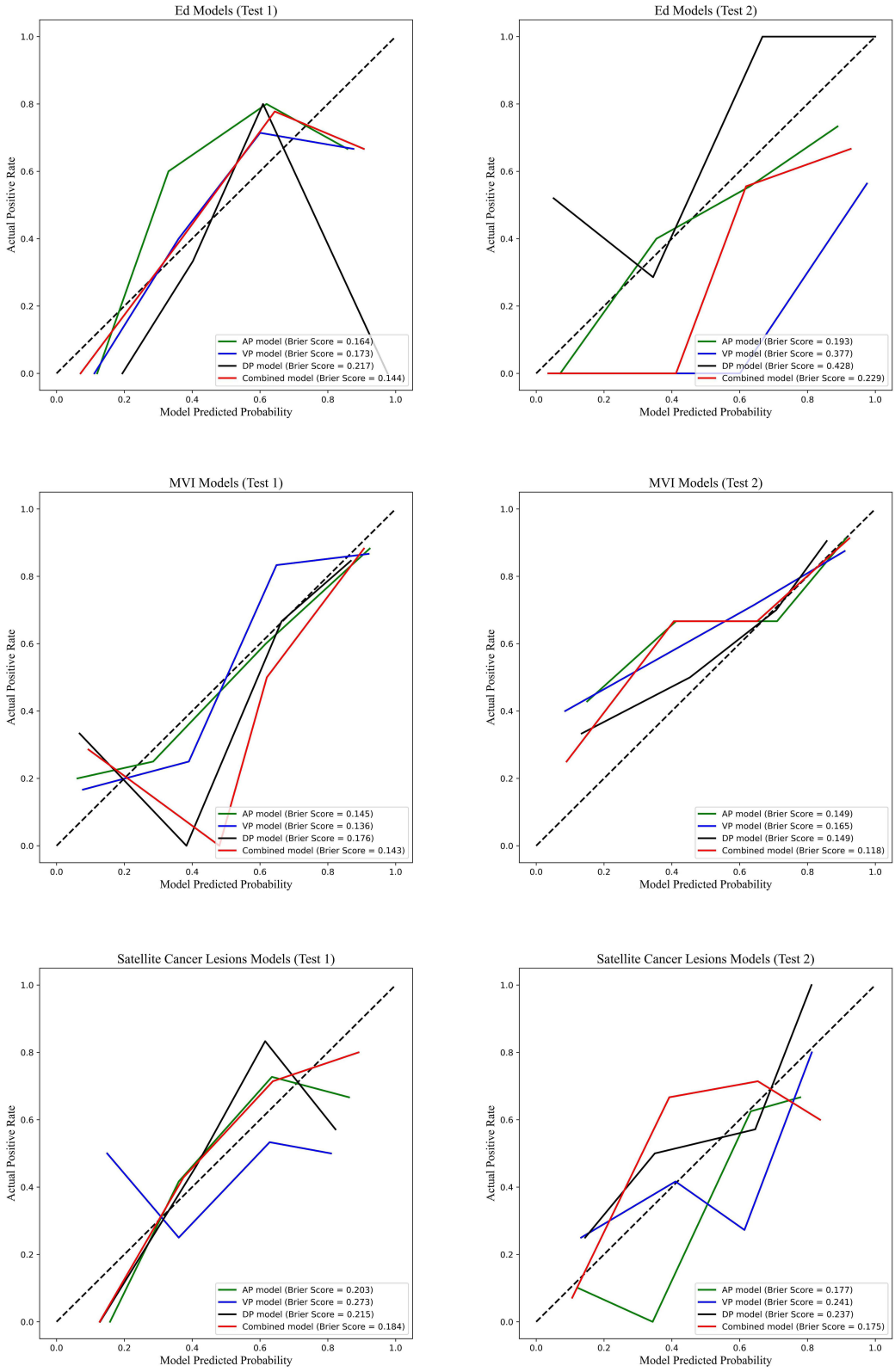

Figure 8 The calibration curves of different models on test 1 and test 2 datasets, respectively. The models for Ed grading, MVI grading, and SN grading (from top to bottom), respectively.

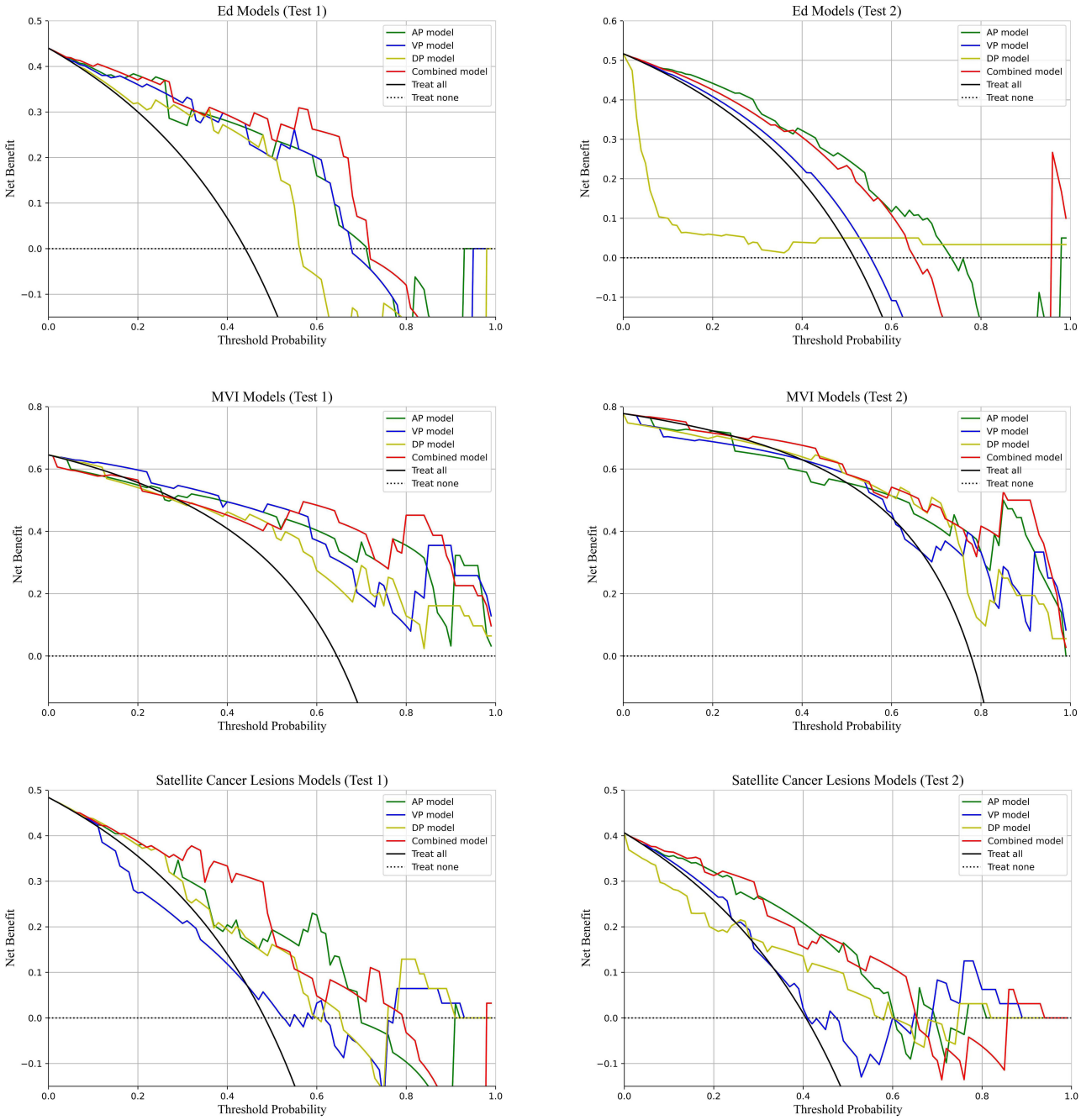

Figure 9 The decision curves of different models on test 1 and test 2 datasets, respectively. The models for Ed grading, MVI grading, and SN grading (from top to bottom), respectively.

Discussion

Biological and Imaging Basis of Arterial Phase Features

Arterial phase hyper enhancement in HCC reflects tumor vascularity, capturing heterogeneous enhancement patterns, linked to angiogenesis and intratumoral necrosis. Key features, like GrayLevelNonUniformityNormalized (textural complexity) and 3D-Kurtosis (peaked intensity distribution) quantify microenvironment heterogeneity. Elevated kurtosis is correlated with necrotic foci and abnormal vascular architecture in high-grade HCC (Ed III–IV).[19] Wavelet-derived features (eg, wavelet-HLL-Large-Area-Low-Gray-Level-Emphasis) further dissect angiogenesis-driven structural disruptions (eg, pseudoglandular tube disintegration), aligning with VEGF overexpression-induced stromal

https://doi.org/10.2147/JHC.S527056

fibrosis.[20] Notably, the DP feature wavelet_glszm_wavelet-HLL-LargeAreaLowGrayLevelEmphasis (LASSO coefficient = 0.0617) outperformed AP 3D-Kurtosis (0.0495) in the Ed prediction, like due to its sensitivity to SN-associated necrosis.[19]

Venous and Delayed Phase Contributions

Venous phase "washout" pattern (Figure 3b) reflect HCC invasiveness. Features like "Original_shape_Maximum2DDiameterSlice_VP" (LASSO coefficient = 0.0828) correlates with microvascular invasion (MVI) risk via spatial expansion.[9] "Zone Entropy_VP" quantifies stromal fibrosis, a hallmark of MVI-positive HCC.[11] Delayed-phase "Long Run Low Gray Level Emphasis" identifies contiguous necrotisis critical for mapping SN-associated microenvironment changes.[21] Delayed-phase "Small Area Low Gray Level Emphasis" (≤2 cm low-gray regions) aligns with SN's pathological definition (SN ≥ 1 satellite nodule within 2 cm), enabling subcentimeter lesions detection.[10]

Synergistic Value of Triphasic Analysis

The fusion model integrates complementary information across phases:

- AP: Captures angiogenesis and cellular atypia.
- VP: Highlights washout patterns linked to MVI (AUC = 0.895).
- DP: Identifies necrotic cores and capsular enhancement (SN AUC = 0.829).

This multi-parametric approach addresses the limitations of single-phase analyses, improving specificity for MVI detection by 12% compared to AP/VP alone.[11] The MVI fusion model integrates three critical phase-specific features: (1) AP wavelet-HHL-DependenceEntropy (reflecting angiogenic hyperinvasiveness); (2) VP Maximum2DDiameterSlice (indicating spatial expansion linked to MVI risk); and (3) DP firstorder_Range (capturing sustained tumor progression). These features collectively cover the full spectrum of MVI pathogenesis—initiation (vascular abnormalities), progression (spatial invasion), and dissemination (continuous expansion)—thereby enhancing predictive performance (AUC = 0.895).

Innovation Data Strengths and Clinical Translation

Core Innovations: Multi-Phase Synergy and Synchronous Prediction

This study introduces two key innovations: First, unlike previous single models (eg, Mao et al.[14] Reported Ed AUC of 0.777 with MRI arterial phase features; Xia et al[15] achieved MVI AUC = 0.760 with single-phase CT), our triphasic fusion model integrates arterial (vascular), venous (washout), and delayed (capsular) phase features, improves Ed AUC to 0.890 (testing 1, +11.3% vs single-phase).[19] Second, its synchronous predict Ed, MVI, and SN—prior studies focused on single markers (eg, Xia et al[15] for MVI; Wu et al[16] for Ed with non-contrast MRI)—providing a one-stop solution for preoperative comprehensive assessment tool, aligning with clinical needs.[18]

Data Strengths: Multi-Center Validation

This study enhances model robustness through multi-center data validation. CT data were collected from two institutions: Center A used a GE Discovery CT 750HD scanner with individualized contrast agent dose (400 mg I/kg) and bolus-triggered AP scanning; Center B used a Siemens SOMATOM Definition Flash scanner with fixed contrast agent dose (1.5 mL/kg) and fixed-delay AP scanning. Despite differences in scanning parameters (eg, reconstruction slice thickness: 1.25 mm vs 1.0 mm), data heterogeneity was reduced via image standardization (uniform abdominal window: 300 HU width/40 HU level; resampling to 1.0 × 1.0 × 1.0 mm^3 isotropic voxels, Table 4), significantly outperforming single-center studies).[9,11]

Clinical Translation: Guiding Decision-Making

The model directly supports clinical practice. For MVI, it predicts with AUC = 0.895 (testing 1), aligning with 2024 consensus guidelines (≥1 cm margins for MVI +),[18] and improves net benefit by 15% vs Single-phase models.[4] For SN

AUC = 0.829 (testing 1) identifies patients for lenvatinib (ORR = 24.1% in SN+ vs 9.2% in SN–).[22] Integrating with BCLC staging refines risk assessment, guiding intensified surveillance for high-risk cases (Ed III–IV, MVI+, SN+), as highlighted by Ji et al.[7]

Synergistic Correlation and Biological Relevance of Pathological Features

Poorly differentiated (Ed III–IV) tumors were significantly correlated with high-risk MVI (M2 grade), SNs, and larger tumor volume (Table 1), consistent with the biological behavior of poorly differentiated tumors being more prone to vascular invasion and metastasis.[4,5] The higher male proportion in the MVI-positive group (91.9% vs 80.4%) may be linked to androgen-driven angiogenic abnormalities;[23] the higher MVI M2 grade proportion in the SN-positive group (60.9% vs 3.1%) suggests shared metastasis-promoting mechanisms (eg, VEGF overexpression).[21] The association of larger tumor volume (>100 cm^3) with all high-risk features (Ed III–IV, MVI+, SN+) ($P < 0.01$) supports the "volume-driven aggressiveness" hypothesis.[24]

Limitations and Future Directions

This study has the following limitations:

1. Sample size constraints for SN prediction: The testing 2 (validation) set for SN prediction included only 32 lesions, which may compromise model stability. Using the DeLong method, the 95% confidence interval (CI) for the SN model's AUC (0.810) in the testing 2 (validation) set was calculated as 0.656–0.963, indicating a relatively wide range of uncertainty. This small sample size limits the generalizability of the SN prediction results. Future studies should expand the SN testing 2 (validation) cohort by collaborating with multi-institutional consortia (eg, the Chinese Liver Cancer Multi-center Collaborative Group) to enhance model robustness and narrow the CI.
2. Simplified pathological grading: The current study used a simplified Edmondson-Steiner classification (Ed I–II vs III–IV). To improve precision, Future research should adopt the WHO 2023 four-tier system, which provides more detailed differentiation grading.

Conclusion

The triphasic CT radiomics model enables synchronous prediction of Ed, MVI, and SN status in HCC patients. Furthermore, the three-phase fusion model shows better performance than single-phase models.

Abbreviations

MVI, Microvascular invasion; SN, Satellite nodule; Ed, Edmondson-Steiner; AP, Arterial phase; VP, Venous phase; DP, Delayed phase; HBP, Hepatobiliary phase; VOIs, Volumes of interest; ICC, Intra-class correlation coefficient; GLCM, Gray-Level Co-occurrence Matrix; GLRLM, Gray-Level Run-Length Matrix; GLSZM, Gray-Level Size-Zone Matrix; GLDM, Gray-Level Dependence Matrix; NGTDM, Neighboring Gray-Tone Difference Matrix; RF, Random forest; ROC, Receiver operating characteristic curve; SEN, Sensitivity; SPE, Accuracy; AUC, Area under the curve; mRMR, minimum Redundancy Maximum Relevance; LASSO, least absolute shrinkage and selection operator (LASSO); AI, Artificial intelligence; ANN, Artificial neural network; DCE, Dynamic contrast-enhanced; LALGLE, Large Area Low Gray Level Emphasis.

Funding

This work was supported by two Self-raised projects by the Health Commission of Guangxi Zhuang Autonomous Region (No.: Z-A20241055; Z20200953).

Disclosure

The authors report no conflicts of interest in this work.

References

1. Siegel RL, Miller KD, Wagle NS, Jemal A. Cancer statistics, 2023. *CA Cancer J Clin*. 2023;73:17–48. doi:10.3322/caac.21763
2. Sung H, Ferlay J, Siegel RL, et al. Global cancer statistics 2020: GLOBOCAN estimates of incidence and mortality worldwide for 36 cancers in 185 countries. *CA Cancer J Clin*. 2021;71:209–249. doi:10.3322/caac.21660
3. Jin J, Jung HY, Lee KH, et al. Nuclear expression of hepatitis B virus X protein is associated with recurrence of early-stage hepatocellular carcinomas: role of viral protein in tumor recurrence. *J Pathol Transl Med*. 2016;50:181–189. doi:10.4132/jptm.2016.03.18
4. Rodriguez-Peralvarez M, Luong TV, Andreana L, Meyer T, Dhillon AP, Burroughs AK. A systematic review of microvascular invasion in hepatocellular carcinoma: diagnostic and prognostic variability. *Ann Surg Oncol*. 2013;20:325–339. doi:10.1245/s10434-012-2513-1
5. Sumie S, Nakashima O, Okuda K, et al. The significance of classifying microvascular invasion in patients with hepatocellular carcinoma. *Ann Surg Oncol*. 2014;21:1002–1009. doi:10.1245/s10434-013-3376-9
6. Sotiropoulos GC, Molmenti EP, Losch C, Beckebaum S, Broelsch CE, Lang H. Meta-analysis of tumor recurrence after liver transplantation for hepatocellular carcinoma based on 1,198 cases. *Eur J Med Res*. 2007;12:527–534.
7. Ji GW, Zhu FP, Xu Q, et al. Radiomic features at contrast-enhanced CT predict recurrence in early stage hepatocellular carcinoma: a multi-institutional study. *Radiology*. 2020;294:568–579. doi:10.1148/radiol.2020191470
8. Lu M, Qu Q, Xu L, et al. Prediction for aggressiveness and postoperative recurrence of hepatocellular carcinoma using gadoxetic acid-enhanced magnetic resonance imaging. *Acad Radiol*. 2023;30:841–852. doi:10.1016/j.acra.2022.12.018
9. Xu X, Zhang HL, Liu QP, et al. Radiomic analysis of contrast-enhanced CT predicts microvascular invasion and outcome in hepatocellular carcinoma. *J Hepatol*. 2019;70:1133–1144. doi:10.1016/j.jhep.2019.02.023
10. Sheng X, Ji Y, Ren GP, et al. A standardized pathological proposal for evaluating microvascular invasion of hepatocellular carcinoma: a multicenter study by LCPGC. *Hepatol Int*. 2020;14:1034–1047. doi:10.1007/s12072-020-10111-4
11. Chen YD, Zhang L, Zhou ZP, et al. Radiomics and nomogram of magnetic resonance imaging for preoperative prediction of microvascular invasion in small hepatocellular carcinoma. *World J Gastroenterol*. 2022;28:4399–4416. doi:10.3748/wjg.v28.i31.4399
12. Meniconi RL, Komatsu S, Perdigao F, Boelle PY, Soubrane O, Scatton O. Recurrent hepatocellular carcinoma: a western strategy that emphasizes the impact of pathologic profile of the first resection. *Surgery*. 2015;157:454–462. doi:10.1016/j.surg.2014.10.011
13. Fan Y, Yu Y, Wang X, Hu M, Hu C. Radiomic analysis of Gd-EOB-DTPA-enhanced MRI predicts Ki-67 expression in hepatocellular carcinoma. *BMC Med Imaging*. 2021;21:100.
14. Mao Y, Wang J, Zhu Y, et al. Gd-EOB-DTPA-enhanced MRI radiomic features for predicting histological grade of hepatocellular carcinoma. *Hepatobiliary Surg Nutr*. 2022;11:13–24. doi:10.21037/hbsn-19-870
15. Xia TY, Zhou ZH, Meng XP, et al. Predicting microvascular invasion in hepatocellular carcinoma using CT-based radiomics model. *Radiology*. 2023;307:e222729. doi:10.1148/radiol.222729
16. Wu M, Tan H, Gao F, et al. Predicting the grade of hepatocellular carcinoma based on non-contrast-enhanced MRI radiomics signature. *Eur Radiol*. 2019;29:2802–2811. doi:10.1007/s00330-018-5787-2
17. Cong WM, Bu H, Chen J, et al. Evidence-based practice guidelines for the standardized pathological diagnosis of primary liver cancer (2015 edition). *Med J Chin PLA*. 2015;11:865–872.
18. Chinese Association of Liver Cancer of Chinese Medical Doctor Association. Chinese expert consensus on the diagnosis and treatment of hepatocellular carcinoma with microvascular invasion (2024 edition). *Chin J Dig Surg*. 2024;23:153–164.
19. Liu HF, Lu Y, Wang Q, Lu YJ, Xing W. Machine learning-based CEMRI radiomics integrating LI-RADS features achieves optimal evaluation of hepatocellular carcinoma differentiation. *J Hepatocell Carcinoma*. 2023;10:2103–2115. doi:10.2147/JHC.S434895
20. Li JJ, Hu DY, Tang H, et al. Study on the correlation of enhancement characteristics in multidetector CT arterial phase with histopathologic differentiation of hepatocellular carcinoma. *Radiol Pract*. 2012;1:61–64.
21. Zhu Y, Weng S, Li Y, et al. A radiomics nomogram based on contrast-enhanced MRI for preoperative prediction of macrotrabecular-massive hepatocellular carcinoma. *Abdom Radiol*. 2021;46:3139–3148. doi:10.1007/s00261-021-02989-x
22. Hu X, Zhou J, Li Y, et al. Added value of viscoelasticity for MRI-based prediction of Ki-67 expression of hepatocellular carcinoma using a Deep Learning Combined Radiomics (DLCR) model. *Cancers*. 2022;14:2575–2585. doi:10.3390/cancers14112575
23. Zaremba AA, Zaremba PY, Zahorodnia SD. In silico study of HASDI (high-affinity selective DNA intercalator) as a new agent capable of highly selective recognition of the DNA sequence. *Sci Rep*. 2023;13:5395. doi:10.1038/s41598-023-32595-4
24. Wagoner CW, Daun JT, Danyluk J, et al. Multiphasic exercise prehabilitation for patients undergoing surgery for head and neck cancer: a hybrid effectiveness-implementation study protocol. *Support Care Cancer*. 2023;31:726. doi:10.1007/s00520-023-08164-w